This is an Accepted Manuscript, which has been through the Royal Society of Chemistry peer review process and has been accepted for publication.

Accepted Manuscripts are published online shortly after acceptance, before technical editing, formatting and proof reading. Using this free service, authors can make their results available to the community, in citable form, before we publish the edited article. We will replace this Accepted Manuscript with the edited and formatted Advance Article as soon as it is available.

You can find more information about Accepted Manuscripts in the Information for Authors.

Please note that technical editing may introduce minor changes to the text and/or graphics, which may alter content. The journal's standard Terms & Conditions and the Ethical guidelines still apply. In no event shall the Royal Society of Chemistry be held responsible for any errors or omissions in this Accepted Manuscript or any consequences arising from the use of any information it contains.

1 **Fluorescence Switching via Competitive ESIPT and Spirolactam Ring**

2 **Opening in a Multifunctional Rhodamine B Probe for Selective Detection of**

3 **Cu²⁺ and OCl⁻: Theoretical Insights with Anticancer and Biosensor Activity**

4 Vishnu Sᵃ Avijit Kumar Dasᵃ* Gouri Karanᵇ, Sujata Maiti Choudhuryᵇ

5 ᵃDepartment of Chemistry, Christ University, Hosur Road, Bangalore, Karnataka, 560029 India

6 *Email: avijitkumar.das@christuniversity.in

7 ᵇCancer Nanotherapeutics Laboratory, Biochemistry, Molecular Endocrinology, and

8 Reproductive Physiology Division, Department of Human Physiology, Vidyasagar University,

9 Midnapore- 721 102, West Bengal, India

10 **Abstract**

11 A multifunctional ESIPT-based rhodamine-derived probe (**BHS**) was synthesized and

12 developed as a colorimetric and fluorometric sensor for the selective detection of copper (Cu^{2+})

13 and hypochlorite (OCl⁻) in aqueous solutions. Initially, **BHS** exhibits intense whitish blue

14 fluorescence due to the active excited-state intramolecular proton transfer (ESIPT) mechanism

15 within the molecule. However, upon interaction with Cu^{2+} and OCl⁻, noticeable changes in

16 absorption and fluorescence occur, attributed to the inhibition of ESIPT resulting from analyte

17 binding with **BHS**, leading to the spirolactam ring opening. Furthermore, significant Stokes

18 shifts in absorption ($\Delta\lambda$ = 34 nm and 170 nm for Cu^{2+}, and 163 nm for OCl⁻) and emission ($\Delta\lambda$

19 = 67 nm for both Cu^{2+} and OCl⁻) further confirm this transformation. The spirolactam ring

20 opening is induced by Cu^{2+} coordination, whereas for OCl⁻, it is triggered by oxidative

21 cleavage. To explore potential biological applications, fluorescence titration experiments were

22 conducted to study the interactions of the **BHS**-Cu^{2+} complex with ct-DNA and the transport

23 protein bovine serum albumin (BSA). Additionally, molecular docking studies were performed

24 to assess these interactions, while DFT calculations were employed to optimize the structures

25 of **BHS** and its Cu^{2+} complex. The fluorescence changes of **BHS** in the presence of Cu^{2+} and

26 OCl⁻ in biological samples has been examined by the anticancer and biosensor activity of **BHS**

27 in HCT-116 colorectal cancer cells.

28

29

30

1. Introduction

Metal ions and anions are essential for a variety of pathological and physiological functions, including catalysis, osmotic control, metabolism, and more. However, it is generally recognized that abnormalities in the concentrations of specific ions in organisms can have a negative impact on normal biological events.[1] In this respect, metal ions, copper is a micronutrient that is necessary for humans, plants and animals. Copper stands in the third position of the most abundant trace metal on earth's crust, behind iron and zinc. Numerous physiological functions, including red blood cell production, maintenance, and healthy development of brain tissues, heart, kidney, and other organs, rely on copper (II) ions.[2,3] Research findings suggest, one of the variables raising the risk of coronary heart disease is copper misregulation. Furthermore, one among the most prevalent contaminants, particularly in drinking water, is Cu^{2+}, in turn degrades water quality and causes a number of illnesses.[4] Additionally, a number of genetic and metabolic diseases in humans, including Parkinson's disease, Alzheimer's disease, Wilson's disease, obesity, diabetes, and others, are brought on by copper dysregulation.[5] The WHO states that the amount of copper ions in drinking water should not exceed more than 31.4μM in order to safeguard human health. [6]

Similarly, one among the most common ROS- reactive oxygen species is hypochlorite (ClO^-). Endogenous hypochlorite is a physiologically significant ROS that is essential to many physiological and pathological processes.[7] It is primarily produced by the innate immune system's myeloperoxidase (MPO)-mediated peroxidation of hydrogen peroxide (H_2O_2) and chloride (Cl^-).[8] It has been demonstrated that an excess of hypochlorite can be harmful and result in conditions including cancer, atherosclerosis, rheumatoid arthritis, fibrillation, and asthma. Cell well-being is majorly dependent on the optimum concentration of hypochlorite. [9] Hence, the development of methods for copper ion and hypochlorite detection has been of utmost importance in environmental and food nutritional fields.

Several techniques have been established for the detection of metallic cations, such as Ion chromatography[10], High-performance liquid chromatography[11], voltammetry[12], electrochemical [13], and ICP-AES - inductively coupled plasma atomic emission spectrometry [14], etc. Although these methods prove to be efficient, they still suffer from certain limitations, such as expensive procedures and instrumentation, complicated operational protocols, and excessive sample pretreatment.[15] In order to overcome these limitations, Fluorescence chemosensors have attracted a lot of interest compared to alternative techniques due to their

63 many benefits, which include ease of device manufacturing, low cost, excellent stability, and

64 quick disposability.[16] Fluorescent chemosensors have the ability to selectively detect several

65 chemical species including cations[17], anions[18], and other compounds, by altering their

66 fluorescence properties. These chemosensors have widely been developed and utilized in the

67 domains of chemistry, life science, environmental research, and materials science due to their

68 high detection sensitivity, rapid analyte response, ease of handling, and ability to facilitate real-

69 time analysis. [19] The rhodamine molecule is a notable example of an off-on type fluorescent

70 probe among the known fluorescent compounds. First created in 1905 by Noelting and

71 Dziewonsky, rhodamine is a class of xanthene-derived dyes used in analytical research initially

72 used for colorimetric detection of a variety of substances, including zinc and silver.[20] Since

73 then, Rhodamine as a scaffold has gained vast significance in analyte detection via colorimetric

74 and fluorometric paths owing to its unique characteristics such as high quantum yields of

75 fluorescence, large molar extinction coefficients, and both long emission and absorption

76 wavelengths.[13] Rhodamine's structure includes a spirolactam ring, which can be observed in

77 two structural forms. The ring opening is generally facilitated upon binding with cations,

78 anions, and certain neutral molecules. While the ring closure spirolactam derivatives are

79 nonfluorescent and colorless, opening of the spirolactam ring results in notable fluorescence

80 changes and a noticeable brilliant pink color.[21] Despite the fact that organic optoelectronic

81 materials have employed a variety of binding mechanisms, the ESIPT- excited-state

82 intramolecular proton transfer phenomenon; a photo-induced proton transfer via an

83 intramolecular hydrogen bond, is of great interest because of its exciting photochemical and

84 photophysical applications.[22]

85
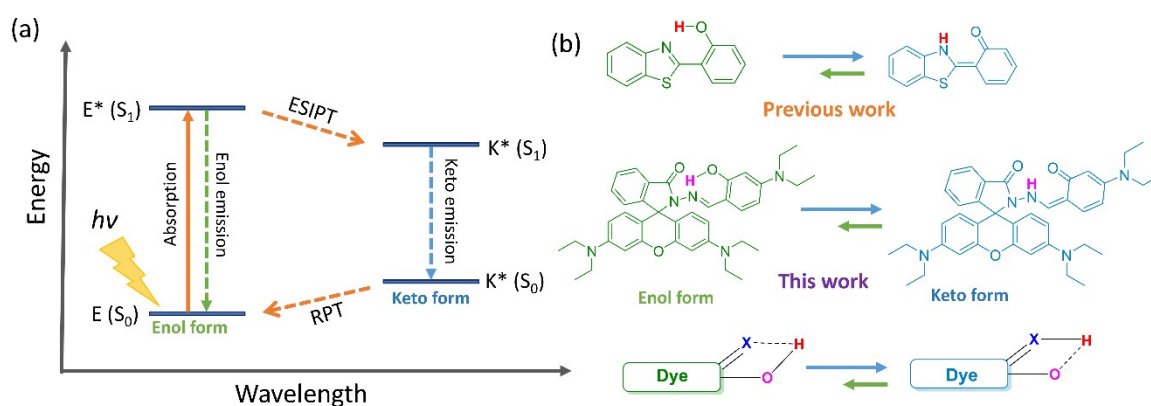
86 **Scheme 1:** (a) Diagrammatic representation of the ESIPT process. (b) Comparison of ESIPT

87 phenomenon with previous work and the current work.

View Article Online
DOI: 10.1039/D5MA00517E

88   The ESIPT process, initially reported in the 1950s by Weller for salicylic acid, has been

89   extensively studied since then for various applications. ESIPT fluorescence occurs when

90   molecules have intramolecular hydrogen bonding between donors and acceptors. ESIPT

91   involves a fast enol-to-keto phototautomerization ($k_{ESIPT} > 10^{12}$ s^{-1}) followed by a radiative

92   decay and reverse proton transfer (RPT) to regenerate the enol form (Scheme 1a). Its significant

93   Stokes shift improves efficiency and helps prevent fluorophores from self-absorbing.[23]

94   Common ESIPT fluorophores include analogues of 2-(2′-hydroxyphenyl)benzimidazole,

95   benzoxazole, and benzothiazole, along with quinoline, benzophenones, flavones,

96   anthraquinones, benzotriazoles, and others.[24] However, these ESIPT chromophores have rarely

97   been coupled with rhodamine-based sensors for analyte detection (Scheme 1b).[25] Therefore,

98   we have designed and synthesized a multifunctional ESIPT based fluorescent probe 3',6'-

99   **b**is(diethylamino)-2-((4-(diethylamino)-2-**h**ydroxybenzylidene)amino)**s**piro[isoindoline-1,9'-

100   xanthen]-3-one (**BHS**) based on the Schiff base condensation reaction of Rhodamine B

101   hydrazide with 4-(Diethylamino) salicylaldehyde derivative for dual detection of cation Cu^{2+}

102   and anion hypochlorite (OCl$^-$). Probe **BHS** has been characterized by NMR and mass

103   spectroscopy (Fig.S1, S2).

104   **2. Experimental section**

105   **Synthetic scheme:**

106
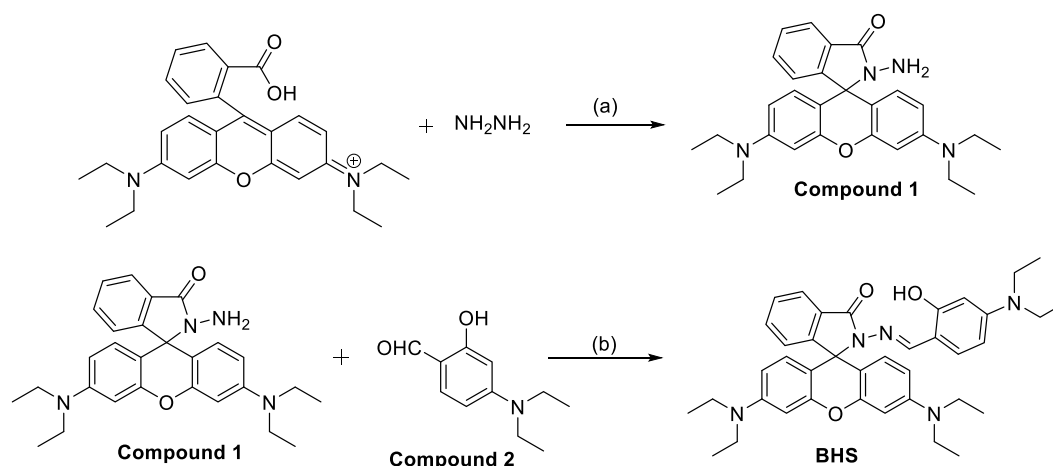
107   **Scheme 2:** (a) MeOH, reflux, overnight. (d) MeOH, rt - 24h.

108   **2.1 Synthesis of rhodamine B hydrazide (compound 1):**

109   The synthesis procedure for **compound 1** was adapted from Dujols et al.[26] The process

110   involved a single-step reaction between rhodamine B and hydrazine hydrate in methanol

111   (Scheme 1). In particular, rhodamine B (0.8 g) was solubilized in 30 ml of methanol, followed

112   by the addition of excess hydrazine hydrate (1 ml). TLC was used to track the reaction mixture's

113   progress while the refluxing continued till the disappearance of the pink color. After the

114   completion of the reaction, the mixture was transferred into ice-cold water and precipitated out

115   a solid pink color. The precipitate was then filtered and let to dry. A solid product yielding a

116   total of 0.54 g (68%) of **compound 1** was obtained.

117   2.2 Synthesis of BHS:

118   The compound **BHS** was synthesized by condensation of rhodamine B hydrazide (**compound**

119   **1**) (236.2 mg, 0.5173 mmol) and 4-(Diethylamino) salicylaldehyde (**compound 2)** (100 mg,

120   0.5175 mmol) in methanol (20 mL) and the mixture was stirred at room temperature for 24 hr.

121   The reaction progress was monitored via TLC. A yellow-colored product was filtered, followed

122   by drying, and it was further recrystallized from ethyl acetate. Yield: 70 mg, 21 %, Mp: 275°C.

123   **^{1}H NMR (CDCl$_3$, 400 MHz):** δ (ppm): 10.94 (s, 1H, -OH), 9.18 (s, 1H, =CH), 7.94 (t, 1H, J

124   = 4 Hz), 7.49 (t, 2H, J = 3.6 Hz), 7.15 (t, 1H, J = 4 Hz), 6.19 (d, 1H, J = 8.4 Hz), 6.47 (q, 4H),

125   6.25 (q, 2H), 6.11 (d, 2H, J = 11.2), 3.31 (q, 12H), 1.41 (q, 18H). **Mass (m/z) :** M$^+$ Calculated

126   for C$_{39}$H$_{45}$N$_5$O$_3$ is 631.35; Found: 633.49 (M+2H)$^+$. **Elemental analysis:** Calculated value: C,

127   74.14; H, 7.18; N, 11.08. Observed value: C, 74.18; H, 7.17; N, 11.05.

128   3. Results and Discussions

129   3.1 Binding study with Cu^{2+} and OCl$^-$

130   To gain insights into the sensing abilities of the synthesized probe **BHS**, emission and

131   absorption studies were conducted with various analytes, including metal ions and anions. The

132   colorimetric and fluorescence properties of **BHS** were analyzed with the addition of various

133   metal ions, like Al^{3+}, Cd^{2+}, Fe^{2+}, Fe^{3+}, Cu^{2+}, Ni^{2+}, Pb^{2+}, Hg^{2+}, Co^{2+}, Mn^{2+}, and Zn^{2+}, in a CH$_3$CN-

134   HEPES buffer (9:1, v/v, pH 7.4). The probe **BHS** initially produced an absorbance peak at 382

135   nm, which, over the addition of Cu^{2+}, exhibited a bathochromic shift resulting in the generation

136   of two strong absorption signals at 416 nm ($\Delta\lambda$ = 34 nm) and 552 nm ($\Delta\lambda$ = 170 nm) along with

137   an isobestic point at 402 nm. This large spectral shift indicates the presence of the ESIPT

138   phenomenon within the molecule. Incremental addition of Cu^{2+} led to a gradual increase in the

139   absorption peak at 552 nm, followed by a noticeable naked-eye color transition, generating

140   pink color from colorless (Fig. 1a). The absorbance of **BHS** changes with the concentration of

141   Cu^{2+} up to the saturation level (Fig. 1b). A linear increase in Cu^{2+} concentration results in a

142   corresponding linear rise in absorbance, which is attributed to the observed color change. The

Materials Advances Accepted Manuscript

emission spectrum of **BHS** alone produced a strong signal at 509 nm when excited at 400 nm. However, after the introduction of Cu^{2+} into the probe solution, a significant decrease in fluorescence intensity at 509 nm was observed along with the emergence of a red-shifted emission signal at 576 nm ($\Delta\lambda = 67$ nm) at a high concentration of Cu^{2+}, which corresponds to the emission signal appearance upon the spirolactam ring opening of rhodamine. Attributing to the **BHS**-Cu^{2+} binding, the fluorescence intensity gradually decreases with increasing concentrations of Cu^{2+} (Fig.1d).
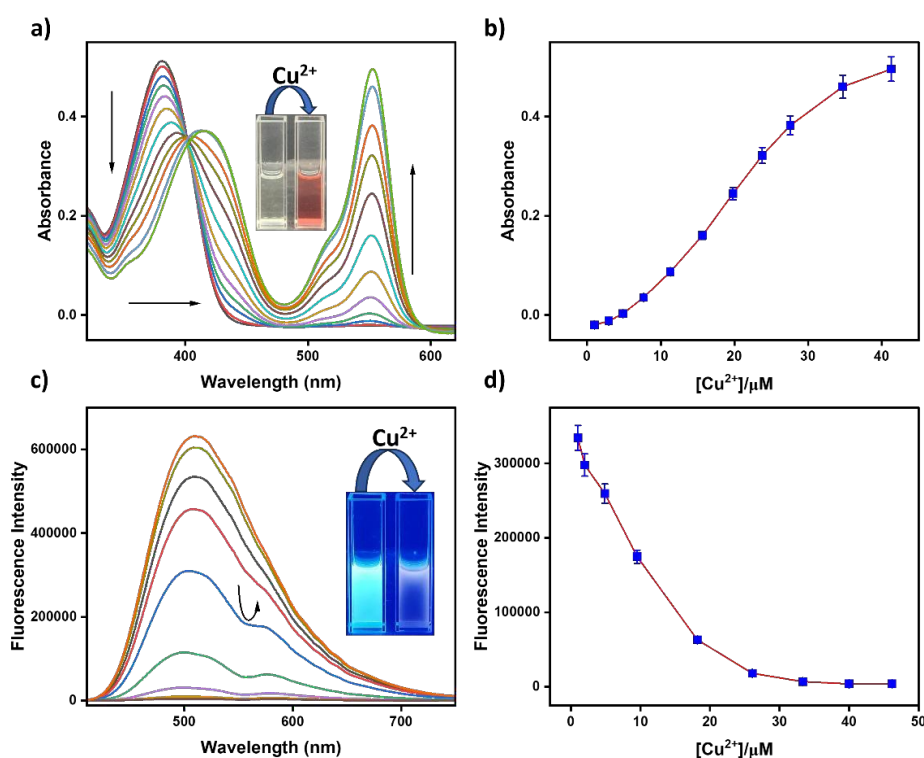

Figure 1. (a) and (c) Colorimetric and fluorometric response of **BHS** ($c = 2\times10^{-5}$ M) with the addition of Cu^{2+} ($c = 2\times10^{-4}$ M, 10 equiv.). (b) and (d) Changes in concentrations vs intensity of **BHS** with Cu^{2+} in absorption and emission titration spectra respectively ($\lambda_{em} = 576$ nm).

Similarly, the UV-*vis* and fluorescence behavior of **BHS** was studied with the addition of several anions, such as Br^-, $C_2O_4^-$, CH_3COO^-, Cl^-, F^-, I^-, H_2O_2, NO_2^-, NO_3^-, OCl^-, and SO_4^2, in CH_3CN-HEPES buffer (9:1, v/v, pH 7.4). The probe **BHS** itself exhibited a single distinct absorption maximum at 382 nm without the addition of any analytes. However, on exposure to OCl^-, a new red-shifted absorption signal emerged at 545 nm ($\Delta\lambda = 163$ nm), which was gradually enhanced with increasing concentrations of OCl^- (Fig. 2a and 2b). This transition was accompanied by a prominent, visually detectable color change from colorless to pink. As a result, a linear increase in absorbance was observed with increasing OCl^- concentrations (Fig.

162   2b). In the fluorescence spectra, the probe **BHS** initially exhibited a strong whitish blue

163   fluorescence with a prominent emission peak at 509 nm. Upon the addition of OCl$^-$, the

164   emission signal exhibited a red shift ($\Delta\lambda$ = 67 nm) to 576 nm from 509 nm followed by the

165   decrease of the emission intensity at 576 nm with the appearance of weak red fluorescence

166   (Fig. 2c and Fig. 2d). The significant stokes shift in the emission spectra also suggests the

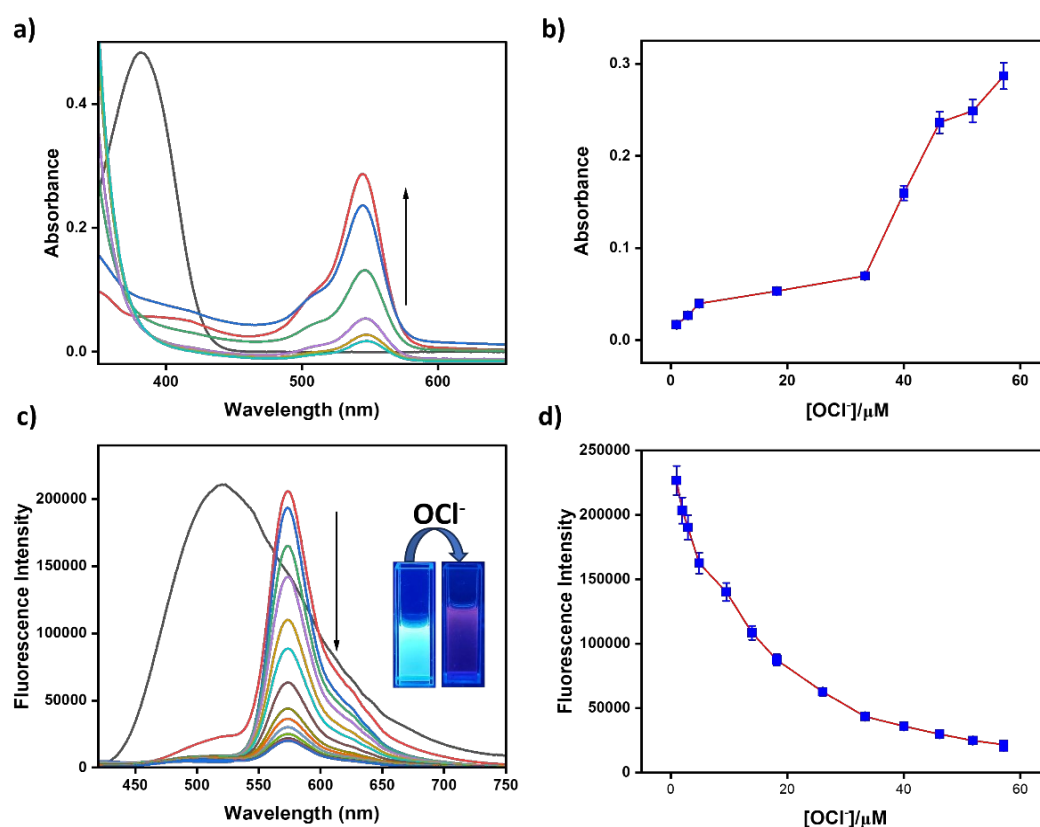167   occurrence of the ESIPT phenomenon within the molecule.

168

169   **Figure 2.** (a) and (c) absorption and emission titration signals of **BHS** (c = 2×10^{-5} M) with the

170   addition of OCl$^-$ (c = 2×10^{-4} M, 10 equiv.). (b) and (d) Concentrations vs. intensity variations

171   of **BHS** with OCl$^-$ in colorimetric and fluorometric titration spectra, respectively (λ_{em} = 576

172   nm).

173   **3.2 Interference study**

174   Interference analysis using colorimetric and fluorometric methods was performed to evaluate

175   the selectivity of **BHS** toward Cu^{2+} by testing various metal ions, including Al^{3+}, Cd^{2+}, Fe^{2+},

176   Fe^{3+}, Hg^{2+}, Mn^{2+}, Ni^{2+}, Co^{2+}, Pb^{2+}, and Zn^{2+}, in CH$_3$CN-HEPES buffer (9:1, v/v, pH 7.4). The

177   probe solution exhibited no notable absorption peak at 552 nm in the presence of different

178   metal ions. Slight interference from Fe^{2+} was observed in the absorption spectra, indicated by

179   the appearance of a pale pink color visible to the naked eye (Fig.3a and 3b). However, upon

180   the addition of Cu²⁺, a prominent signal appeared at 552 nm, attributed to the formation of a

181   distinct pink color from the initially colorless probe solution. The naked eye visible color

182   change appeared selectively in presence of Cu²⁺ (Fig.3a) with the appearance of the

183   corresponding strong UV-*vis* absorption signal (Fig.3b), while Fig. 3c presented a bar graph of

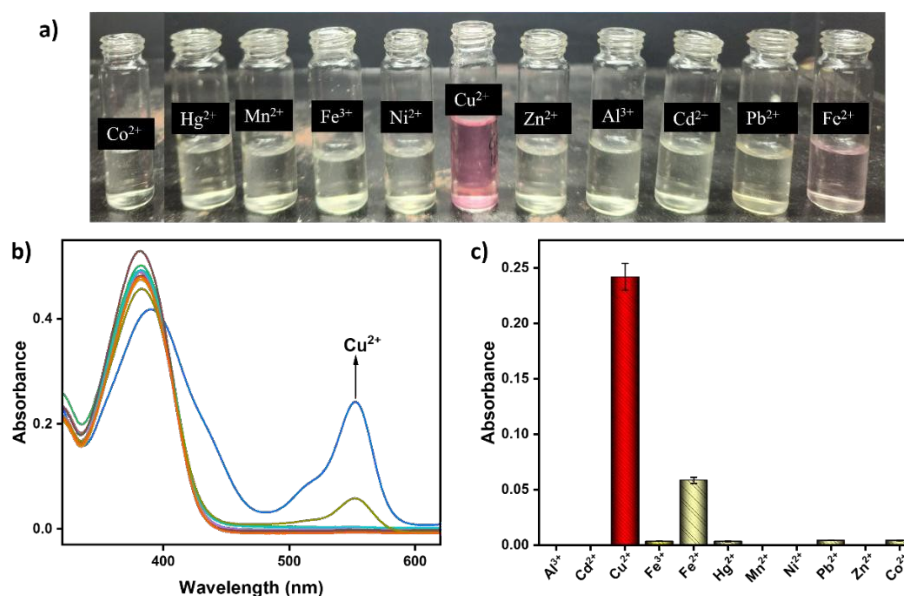184   the absorption intensities, with the red bar representing the solution containing Cu²⁺.

185

186   **Figure 3.** (a) Naked eye colour changes of probe **BHS** with several metal ions. b) Colorimetric

187   behaviour of **BHS** on exposure to diverse metal ions (10 equiv.) in CH_3CN–aqueous HEPES

188   buffer solution (9/1, v/v, pH = 7.4). (c) Absorption intensity changes of the sensor **BHS** upon

189   introduction of the interfering metal ions ($c = 2 \times 10^{-4}$ M, 10 equiv.).

190   Similarly, fluorometric titration analysis revealed that no metal ion induced significant changes

191   in the probe solution, except for Cu²⁺. This metal ion Cu²⁺, along with displaying a prominent

192   quenching of fluorescence intensity at 509 nm, produced a secondary signal at 576 nm, which

193   can be attributed to the binding interaction between **BHS** and Cu²⁺ (Fig.4). The fluorescence

194   quenching phenomena paving the way to the emergence of new fluorescence, as observed

195   under a UV chamber (Fig. 4a). The emission spectrum of **BHS** with various metals ions has

196   been shown in the interference study, wherein the signal of emission at 509 nm was unaffected

197   with the presence of any other interfering cations except for Cu²⁺ but minor interference from

198   Co²⁺ was detected in the fluorescence spectra (Fig. 4b). While bar graph representation displays

199   the same observation on exposure to several interfering metal ions and the lower intensity red

200   bar indicates emission response of **BHS** in presence of Cu²⁺ at 509 nm (Fig.4c).
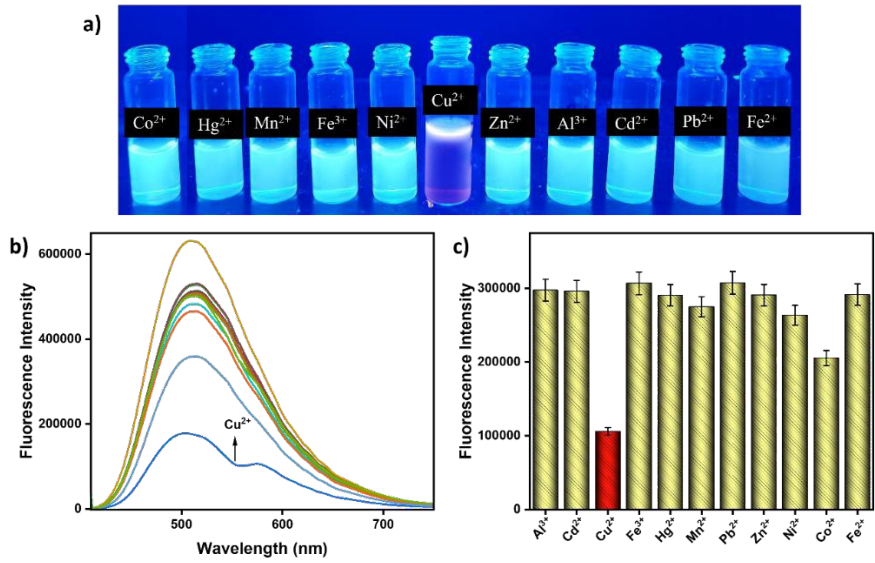
201

202

Figure 4. (a) Fluorescent properties of probe **BHS** with various cations under UV light. b) Fluorescence signal of **BHS** on the addition of various cations (10 equiv.) in CH_3CN–aqueous HEPES buffer solution (9/1, v/v, pH = 7.4). (c) Changes in fluorescence intensity of the sensor **BHS** with the addition of other interfering cations ($c = 2 \times 10^{-4}$ M, 10 equiv.).

Similarly, the interference analysis of **BHS** with various anions, including Br^-, $C_2O_4^{2-}$, CH_3COO^-, Cl^-, F^-, I^-, $H_2O_2^-$, NO_2^-, NO_3^- and SO_4^{2-}, was conducted in CH_3CN-HEPES buffer (9:1, v/v, pH 7.4). Only exposure to OCl^- produced significant changes in absorbance and emission intensities at 545 nm and 576 nm, respectively. The absorption spectrum displayed a distinctive peak at 545 nm, while the fluorescence spectrum exhibited a new, selective signal at 576 nm exclusively with OCl^-. No notable changes in absorbance or emission were observed in the presence of several other anions (Fig. 5 and 6). Followed by bar graph depiction of the same, wherein the selective behavior of **BHS** toward OCl^- is highlighted with a pink bar of higher intensity compared to the lower-intensity yellow bars for other anions in the absorption study (Fig. 5c). Similarly, in the fluorescence study, a lower-intensity bar (pink) represents OCl^-, contrasting with higher-intensity bars (yellow) for other anions (Fig. 6c). All these results demonstrate the selective interaction of **BHS** with Cu^{2+} and OCl^- against all the interfering metal ions and anions.
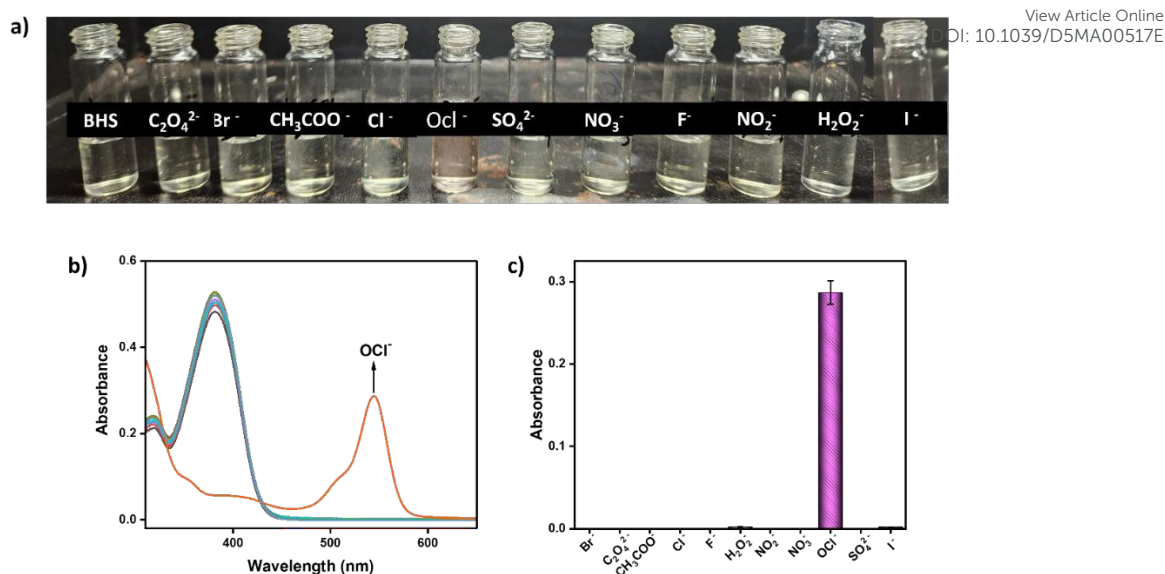
Figure 5. (a) The changes of naked eye color of the probe **BHS** with several anions. b) Absorption behaviour of **BHS** upon addition of several anions (10 equiv.) in CH$_3$CN–aqueous HEPES buffer solution (9/1, v/v, pH = 7.4). (c) Absorption intensity changes of the probe **BHS** upon the addition of interfering anions ($c = 2 \times 10^{-4}$ M, 10 equiv.).
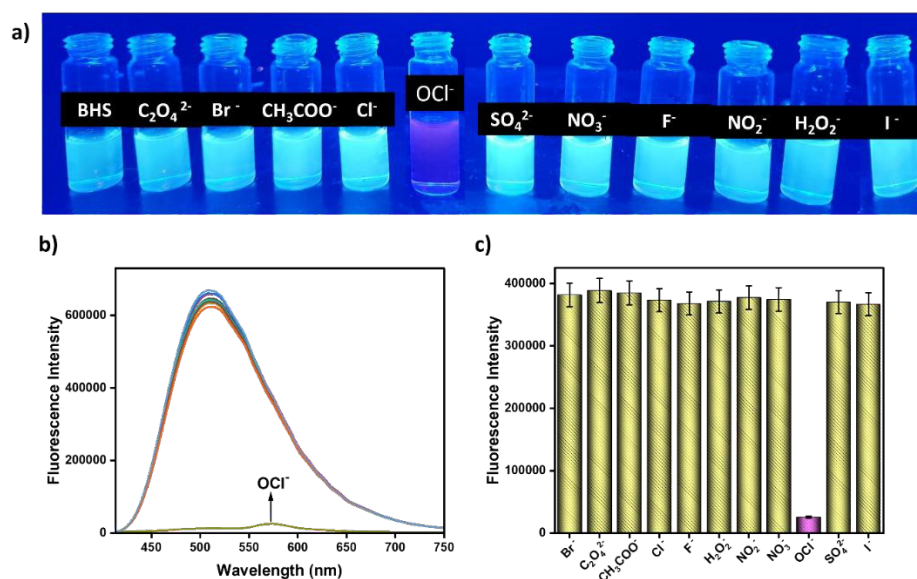

Figure 6. (a) Fluorescent properties of ligand **BHS** with different anions under UV light. b) The fluorescence spectra of **BHS** with the addition of several anions (10 equiv.) in CH$_3$CN–aqueous HEPES buffer solution (9/1, v/v, pH = 7.4). (c) Changes of fluorescent intensity of the sensor **BHS** with the addition of various interfering anions ($c = 2 \times 10^{-4}$ M, 10 equiv.).

10

232 **3.3 Competition study**

233 Furthermore, a competition study was conducted to analyze the selective binding abilities of

234 **BHS** toward Cu^{2+} and OCl^- against several other competing cations and anions, respectively,

235 in CH_3CN-HEPES buffer (9:1, v/v, pH 7.4). The absorption spectra demonstrate the selectivity

236 of **BHS** for Cu^{2+} (red bars) and OCl^- (pink bars), with the emergence of prominent peaks at 552

237 nm and 545 nm, respectively, even in a competing ionic environment (Fig.7a and 7b). This

238 indicates minimal competition effects on the efficiency of **BHS** towards selective detection of

239 Cu^{2+} and OCl^-. Furthermore, the fluorescence titrations showed that Cu^{2+} and OCl^- selectively

240 quenched the fluorescence of **BHS**. The high fluorescence intensity (yellow bars) represents

241 the signal of **BHS** with individual ions, whereas, in the presence of Cu^{2+} (red bars) and OCl^-

242 (pink bars), a notable decrease in fluorescence intensity at 576 nm was observed, confirming

243 the selective detection of target analytes. These results further assert the strong selectivity of

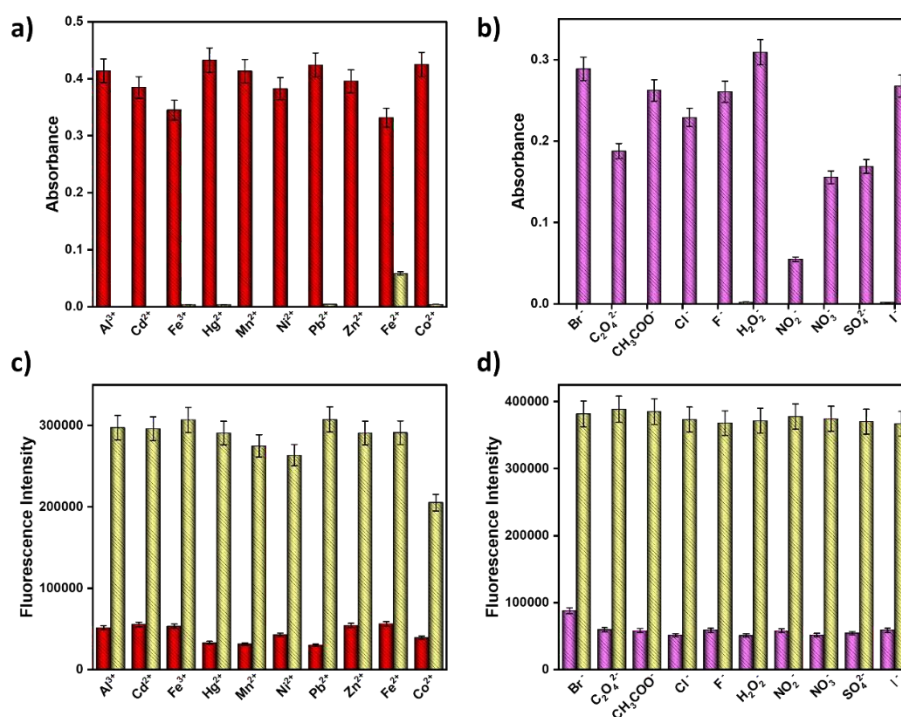244 **BHS** for Cu^{2+} and OCl^- (Fig. 7c and 7d).

245

246 **Figure 7.** (a) and (c) Changes in colorimetric and fluorometric spectra of **BHS** ($c = 2 \times 10^{-5}$M)

247 upon the addition of several metal ions ($c = 2 \times 10^{-4}$M, 10 equiv.) (golden bars); changes in

248 emission behaviour of these interfering metal ion signals against the addition of Cu^{2+} (red bars).

249 (b) and (d) Change in colorimetric and fluorometric spectra of **BHS** ($c = 2 \times 10^{-5}$M) upon

250 addition of several anions ($c = 2 \times 10^{-4}$M, 10 equiv.) (golden bars); changes in emission

251 behaviour of these interfering anions against the addition of OCl^- (pink bars).

252   On the basis of the fluorometric studies of **BHS** with Cu^{2+} and OCl^-, the limit of detection of

253   the probe **BHS** for Cu^{2+} and OCl^- were determined as 6.3 μM and 8.21 μM respectively,

254   utilizing the formula DL= K ×Sb_1/S, where K = 3, Sb_1 is the standard deviation of the blank

255   solution, and S is the slope of the calibration curve (Fig.S5 & S6) [27]. At 552 nm, the molar

256   absorption coefficient for **BHS** and **BHS** - Cu^{2+} were calculated as 10.57×10^3 mol^{-1}-liter-cm^{-1}

257   and 2.48×10^3 mol^{-1}-liter-cm^{-1}. Through the Jobs plot analysis, the 1:1 binding stoichiometry

258   for **BHS** –Cu^{2+} complexation was verified and from the fluorescence titration experiment, the

259   association constant (K_a) of **BHS** with Cu^{2+} was calculated as 2.7×10^5 M^{-1} (error < 10%)

260   (Fig.S9). [28,29] To further evaluate the probe's stability and sensing capabilities across different

261   pH environments, UV-vis experiments were conducted. Notably, the sensor **BHS** exhibited an

262   intense naked-eye-visible color in strongly acidic conditions, accompanied by a strong

263   absorption signal at 552 nm, while no response was observed in neutral or basic media. This

264   indicates that the spirolactam ring opens in acidic environments without the addition of metal

265   ions, whereas it remains stable in neutral and basic media. However, in the presence of Cu^{2+},

266   the spirolactam ring also opens under neutral and basic conditions (Fig. S11). Therefore, to

267   simulate physiological conditions, the sensing behavior of **BHS** with Cu^{2+} and OCl^- was

268   studied at pH 7.4 using HEPES buffer.

269   **3.4 Reversibility study**

270   A fluorometric analysis was performed to assess the reversibility of the binding interaction

271   between **BHS** and Cu^{2+}, providing further insights into the binding properties of **BHS** with

272   Cu^{2+}. The intensity of fluorescence gradually increased upon incremental addition of H_2S to

273   the **BHS**-Cu^{2+} complex, indicating the reversible binding behavior of **BHS** with Cu^{2+} (Fig. 8).

274   The notable fluorescence enhancement suggests that H_2S extracts Cu^{2+} from the **BHS**-Cu^{2+}

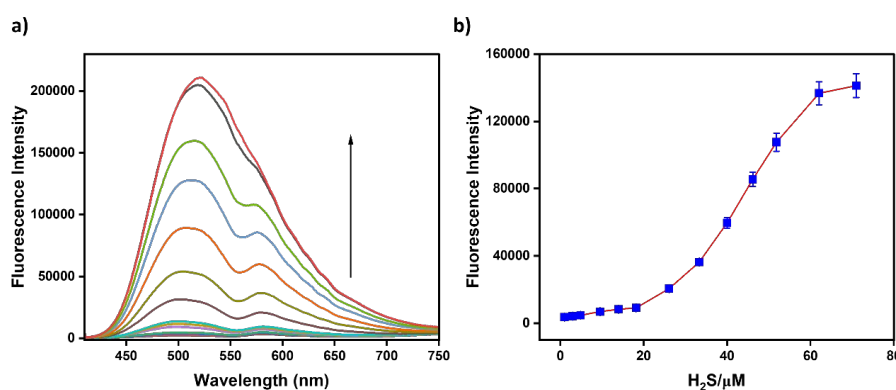275   complex, releasing the free probe **BHS** and confirming its reversible metal ion binding.

276

277 **Figure 8.** (a) Emission behaviour of **BHS-Cu^{2+}** ($c = 2\times10^{-5}$M) with the addition of H$_2$S solution

278 ($c = 2\times10^{-4}$M). (b) Emission intensity changes of the **BHS-Cu^{2+}** complex as a function of the

279 H$_2$S concentration.

280 **3.5 Probable binding mode**

281 Without the presence of analytes, the ligand **BHS** alone exhibits strong whitish blue

282 fluorescence due to the conversion of enol intermediate to the keto form through an ultrafast

283 photo-induced tautomerization process via Excited-state intramolecular proton transfer

284 (ESIPT). This process involves the transfer of a proton from the acidic hydroxyl group to the

285 basic imine nitrogen, facilitated by the formation of a six-membered transition state (Pathway

286 a, Scheme 3). As a result, **BHS** shows strong absorbance signal at 382 nm and emission signal

287 at 509 nm with notable stokes shifts about 127 nm. Moreover, large spectral shifts of absorption

288 ($\Delta\lambda = 34$ nm and 170 nm for Cu^{2+} and 163 nm for OCl$^-$) and emission signals ($\Delta\lambda = 67$ nm for

289 Cu^{2+} and OCl$^-$) of **BHS** on binding with Cu^{2+} and OCl$^-$ suggests the occurrence of the ESIPT

290 phenomenon within the molecule.[30] But, the changes in absorption and fluorescence upon

291 exposure to Cu^{2+} and OCl$^-$ are attributed to the suppression of ESIPT due to analyte binding

292 with **BHS**, followed by spirolactam ring opening. For Cu^{2+}, this occurs through metal ion

293 coordination, while for OCl$^-$, it is driven by oxidative cleavage. During the interaction, a ring

294 strain is influenced within the molecule due to the high Lewis acid strength of copper and its

295 coordination with nitrogen and oxygen donor centers in **BHS**. The Cu^{2+} chelation with the

296 rhodamine-linked derivative **BHS** triggers a chelation-enhanced fluorescence (CHEF) "off-on"

297 colorimetric and fluorometric response (Pathway b, Scheme 3). This transformation involves

298 the translation of the colorless, non-fluorescent spirolactam structure **BHS** to the ring-open

299 form, **BHS1**, which exhibits strong fluorescence and pink color. Spectroscopic analyses,

300 including mass spectrometry and DFT studies, support this mechanistic transformation. The

301 **BHS1** and Cu^{2+} complex formation was confirmed by the appearance of a mass peak at $m/z =$

302 735.50 (Fig.S3), corresponding to [**BHS**-Cu^{2+}-CH$_3$CN]$^+$ (Fig. S4, ESI). A 1:1 binding

303 stoichiometry has been confirmed through the Job's plot analysis and further corroborated by

304 DFT analysis (Fig. S8). The opening of the spirolactam ring of rhodamine derivative is

305 responsible for the changes of absorption and emission color of **BHS** upon the addition of OCl$^-$.

306 Coordination of metal ions such as Cu^{2+} with the rhodamine moiety usually results in ring

307 opening without any loss of groups from the binding site of rhodamine derivative.

308 Nevertheless, in the presence of water, OCl$^-$ oxidizes the hydrazide group of **BHS**, leading to

309 the formation of pink-colored, red fluorescent rhodamine-b itself (**BHS2**) (Pathway c, Scheme

310 3). This transformation is confirmed by the presence of a mass peak at m/z = 444.02

311 corresponding to mass of rhodamine-B (Fig.S4).

312
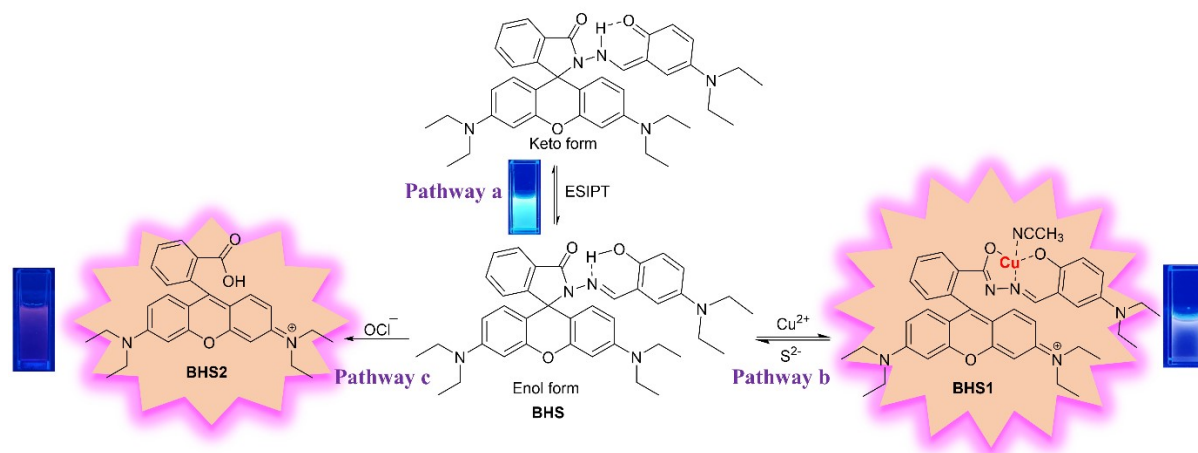
313 **Scheme 3:** Plausible binding of **BHS** with Cu^{2+} and OCl^- in solution phase.

314

315 **3.5 Dipstick method**

316 To analyze the real-time applicability of the probe, test strips were created by initially treating

317 TLC plates with the synthesized receptor solution of **BHS** ($c = 2\times10^{-5}$M). Further upon

318 exposure of analytes OCl^- and Cu^{2+} to the test kits that had been pre-treated with the **BHS**

319 probe, significant color changes were observed attributed to the detection capabilities of the

320 probe (Fig.9). These test strips, often referred to as dipsticks, have proved efficacy in delivering

321 prompt qualitative results without requiring any kind of complex instrumental examination.
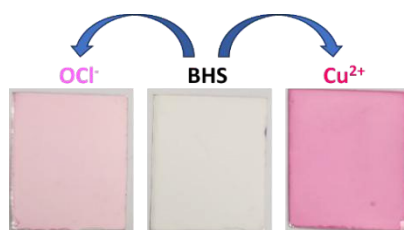

322

323 **Figure 9**. Color changegs of the **BHS** treated TLC plates ($c = 2 \times 10^{-5}$ M) with an exposure to

324 Cu^{2+} and OCl^- ($c = 2 \times 10^{-4}$ M).

325

326 **3.6 Biological Applications**

327 **3.6.1 DNA Binding Study**

328 Fluorometric analysis was performed in order to evaluate the binding abilities of the metal-

329 ligand complex along with duplex ct-DNA in a buffer medium of Tris–HCl (pH 7.2). The

330 fluorescence signal corresponding to BHS-Cu^{2+} complex exhibited quenching upon

331 progressive addition of ct-DNA (Fig. 10a and 10b). The gradual reduction in fluorescence

intensity at 576 nm over increasing additions of ct-DNA is attributed to the binding interaction between metal-ligand complex and ct-DNA. Generally, upon binding with metal ions, the BHS-Cu^{2+} complex adopts a more rigid and sterically constrained structure, which hinders its ability to intercalate between the tightly packed DNA base pairs. Instead, it predominantly associates with the DNA grooves, especially the minor groove, where it can establish hydrogen bonding, van der Waals interactions, and electrostatic attractions with the DNA backbone. These interactions are more energetically favorable and accessible for the rhodamine-metal complex, resulting in groove binding rather than intercalation.[31] The detection limit for the fluorometric measurements of the DNA binding studies was determined to be 13.15 µM (Fig. S7a). Based on the fluorometric experiments, the binding constant (K_b) of BHS-Cu^{2+} towards ct-DNA was calculated as 9.2×10^4 M^{-1} using a non-linear binding isotherm (Fig. S10a).
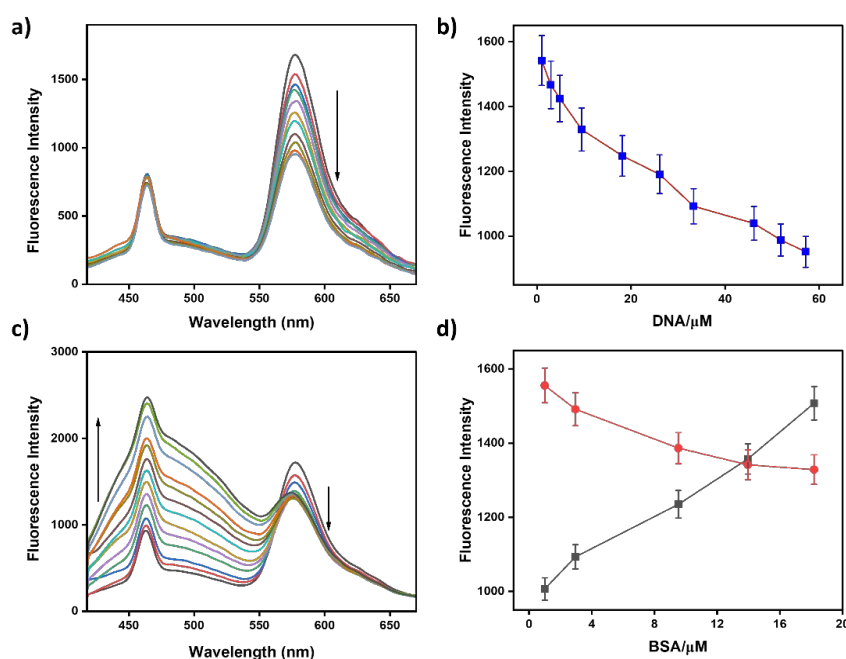

Figure 10. Emission spectra of BHS-Cu^{2+} complex ($c = 2.0 \times 10^{-5}$ M) over serial increments of (a) ct-DNA (c = 2mM in base pairs) and (c) BSA (c = 7.4µM) both in a buffer medium of Tris–HCl (pH 7.2) respectively. Changes emission intensity of the complex (λ_{em} = 576 nm) with respect to (b) ct-DNA and (d) BSA concentrations.

3.6.2 Protein Binding Study

Furthermore, the probe BHS was analyzed for its binding capability towards bovine serum albumin (BSA) in a buffer medium of Tris–HCl (pH 7.2) using fluorescence titration studies. The emission spectrum of the BHS-Cu^{2+} metal-ligand complex exhibited two distinctive peaks: a relatively low-intensity signal at 463 nm and a higher-intensity signal at 576 nm (Fig. 10c).

353   Interestingly, upon the serial addition of BSA to the complex, the fluorescence titration resulted

354   in a ratiometric peak; the peak intensity at 463 nm progressively enhanced, whereas the higher-

355   intensity peak at 576 nm displayed gradual quenching. The detection limit for the protein-

356   binding study was calculated to be 23.08 µM using fluorometric analysis (Fig. S7b) and based

357   on based on a non-linear fluorometric binding isotherm, binding constant (K_b) of the **BHS**-Cu^{2+}

358   complex with BSA was determined to be 5.9×10^4 M^{-1} (Fig. S10b).

359   **3.6.3 *In vitro* cytotoxicity study on HCT-116 cells by MTT assay**

360   Dose-dependent cytotoxicity of **BHS** was determined against HCT-116 colorectal cancer cells

361   by MTT assay. Soluble tetrazolium salt (yellow) is converted to purple formazan crystals by

362   viable cells.[32] Based on this principle, it was found that **BHS** was able to produce significant

363   toxicity in HCT-116 cells. The IC_{50} dose of 115.48 µM was calculated from the dose-effect

364   curve, where cell viability was reduced to 50% of the control population. At the highest

365   concentration dose of 250 µM, cell viability was reduced up to 27.29 % (Fig. 11), which

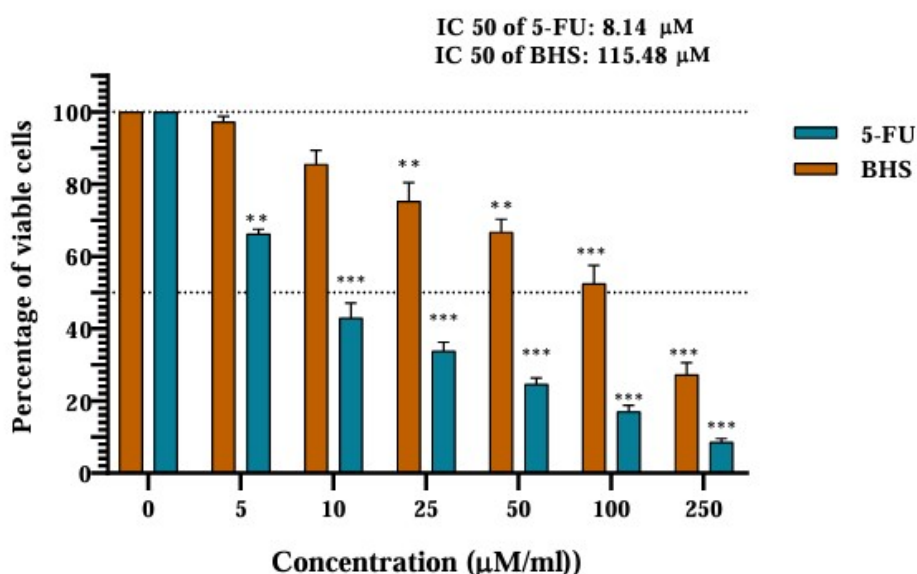366   strongly denotes the potent anticancer activity of **BHS** against HCT-116 cells.

367

368   **Figure 11.** A bar diagram of HCT-116 cell viability at different dosage concentrations of **BHS**.

369   Calculated IC $_{50}$ of **BHS** and 5-FU were 115.48 and 8.14 µM, respectively. Data are presented

370   as mean ± SEM of three independent experiments. '**', '***' represents significant difference

371   in cell viability compared to control HCT-116 cells at $p<0.01$, $p<0.001$ respectively.

372   **3.6.4 Fluorescence imaging study**

373   Fluorescence activity of ligand **BHS** in the presence of sensing analytes copper (Cu^{2+}) and

374   hypochlorite (OCl^-) was studied on the HCT-116 colorectal cancer cell line. Significant

375 fluorescence shifting from 500 nm to 580 nm wavelength in the presence of analytes, denoted

376 as efficient sensitivity of **BHS** for Cu^{2+} and OCl^- detection in biological samples. HCT-116

377 cells showed prominent emission of blue fluorescence near the 500 nm region, after 6 hours

378 incubation with **BHS**, indicating endocytosis-mediated internalization of **BHS** in the cell

379 cytoplasm. On the other hand, after further incubation with exogenous copper ($Cu^{2+)}$) and

380 hypochlorite (OCl^-), a significant reduction in blue fluorescence intensity was observed in

381 HCT-116 cells. However, red fluorescence emission was more prominent in the 580-600 nm

382 region after Cu^{2+} and OCl^- treatment (Fig.12). The data indicate a shift in fluorescence pattern

383 from **BHS** from blue to red due to the formation of the ligand-analyte complex and alteration

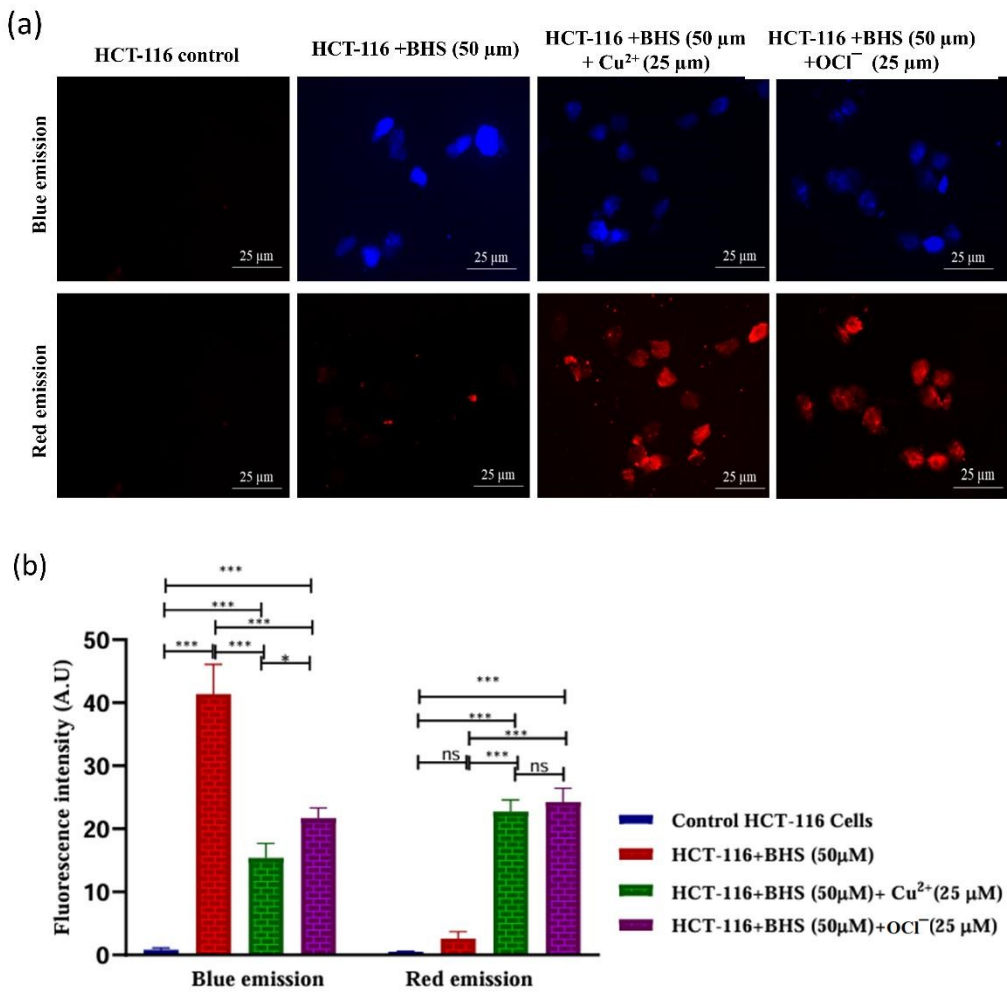384 in electron transition.

385

386

387 **Figure 12.** (a) A fluorescence imaging study of HCT-116 colorectal carcinoma cells after the

388 respective treatment strategy. HCT-116 cells treated with **BHS** showed significant blue

389 fluorescence intensity at 500 nm wavelength, while significant ($p<0.001$) red fluorescence

390 emission near the 580-600 nm region was observed after incubation with exogenous Cu^{2+} and

391 hypochlorite (OCl^-) analytes. **BHS**-treated cells showed negligible red fluorescence emission

392 due to the intracellular low concentration of cuprous and hypochlorite ions.   The images

393 (Magnification 400X) were captured by a fluorescence microscope (Leica DFC 295, Germany)

394 using UV and green excitation filters. (b) The bar diagram represents relative fluorescence

395 intensity expressed as Mean ± SEM of three independent experiments. '*', '**', '***'

396 represents significant difference in cell viability compared to control HCT-116 cells at $p<0.05$,

397 $p<0.01$, $p<0.001$ respectively.

3.7. Theoretical applications

3.7.1 DFT study

400 In order to elucidate the coordination chemistry of Cu^{2+}-**BHS**, structural optimizations using

401 the DFT; density functional theory method for both **BHS** and its Cu-complex were conducted

402 at the B3LYP level (Fig. 13a). Initially the basis set 6–31G (d, p) was applied for the simple

403 receptor (**BHS**), while the basis set LANL2DZ was employed for the Cu^{2+} complex. The

404 Gaussian 09 software package was used to perform the calculations. Additionally, the spatial

405 distribution of electron clouds was analyzed, and computed orbital energies of HOMO; highest

406 occupied molecular orbital and LUMO; lowest unoccupied molecular orbital for both Probe

407 and its metal-complex. The HOMO in **BHS** was analyzed to be primarily localized within the

408 spirolactam ring, whereas the LUMO was analyzed to be extended across the molecule (Fig.

409 13c). These findings imply that the opening of the spirolactam ring could have enhanced

410 coordination involving the ionophore carbonyl oxygen, the oxygen of diethyl amino

411 salicylaldehyde, and Cu^{2+}. Cu^{2+} coordinates with **BHS** through four coordination sites,

412 including one nitrogen from the hydrazide group, two oxygen atoms from the carbonyl and

413 hydroxyl groups of salicylaldehyde, and a single nitrogen from the acetonitrile solvent,

414 adopting a square planar geometry according to the optimized structure of **BHS**-Cu^{2+} complex.

415 The calculated Cu-O bond lengths for the phenolic and hydrazide moieties were 1.99 Å and

416 2.09 Å, respectively, while the Cu-N bond lengths for the acetonitrile and hydrazone nitrogen

417 atoms were 1.89 Å and 1.96 Å, respectively. Bond angles involving imine nitrogen, Cu,

418 phenolic oxygen, and hydrazide oxygen were determined to be 88.84° and 83.12°, while those

419 involving acetonitrile nitrogen, Cu, phenolic oxygen, and hydrazide oxygen were 91.15° and

420 96.87° (Fig.13b).

421 On further analysis of the metal-complex it was found that, the π-electrons in HOMO were

422 predominantly confined near the metal center, while the LUMO was localized to the xanthene

423 moiety. Following this the energy gap calculations were performed, wherein the gap between

424   HOMO (-4.650 eV) and LUMO (-0.957 eV) for **BHS** was calculated as 3.69 eV. Whereas the

425   **BHS**-Cu complex, energy gap was increased to 6.42 eV (HOMO = -6.901 eV, LUMO = -0.476

426   eV). From the TD-DFT study of **BHS**-Cu complex, one of the experimental absorption signals

427   appeared at 416 nm, which is so close to the theoretical TD-DFT calculated absorbance

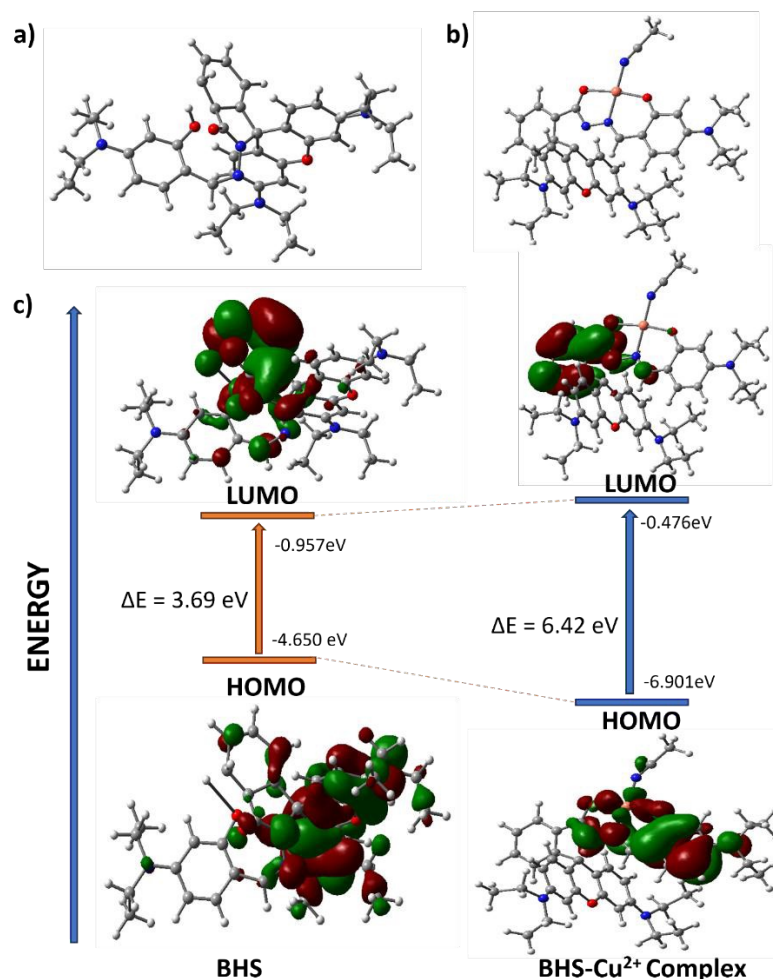428   appeared at 413.83 nm for S0 to S5 transition (Energy: 2.996 eV, f = 0.0015).

430   **Figure 13.** Optimized Geometrical molecular structure of both (a) **BHS** and (b) **BHS** - Cu^{2+}

431   complex. (c) Frontier molecular orbital and the energy differences of the **BHS** and **BHS** - Cu^{2+}

432   complex.

433

434   **3.7.2 In silico molecular docking studies**

435   The molecular docking analysis was utilized to further explore the binding interactions of **BHS**-

436   Cu^{2+} complex with the ct-DNA and BSA protein. It is a technique that has been widely proven

437   to be effective in predicting the possible binding site and the affinity of metal complexes with

438   biomolecules, such as DNA and proteins.[32] This molecular docking analysis was performed

439   with the Autodock Vina application (Fig.14). The **BHS** - Cu^{2+} complex exhibited strong

440 binding with the BSA protein (Fig. 14a) through amino acid residues such as GLU125,

441 LYS136, ARG185, PHE133, TYR137, PRO117, LEU122 and others with a binding affinity of

442 -19.6 kcal/mol. Similarly, the molecular docking study of the of **BHS-Cu^{2+}** complex with ct-

443 DNA also helped in calculating the binding affinity of the ligand interaction with the DNA

444 double helix to be -11.5 kcal/mol (Fig. 14b). These Interactions between the metal complex

445 and the double helix DNA molecule were established through Cytosine [Cyt7, Cyt16, Cyt17],

446 Adenosine [Ade8], Thymidine [Thy9], and Guanosine [Gua14, Gua15] nucleotides. On

447 analysing the above-mentioned docking results, we can conclude that, the **BHS**-Cu^{2+} complex

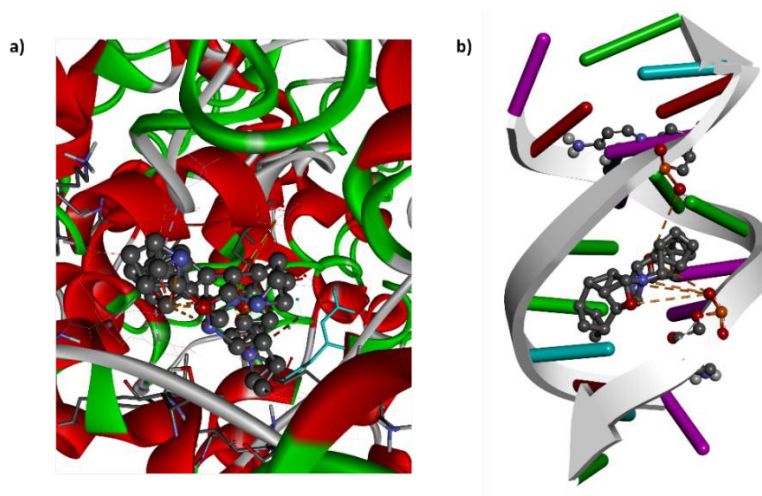448 has been established to possess a greater binding affinity towards DNA and BSA.

449

450 **Figure 14.** Plausible binding mechanisms of the **BHS**-Cu^{2+} metal complex with (a). BSA and

451 (b) ct- DNA complexes, respectively in ribbon view.

452

453 **3.8. Conclusion:**

454 In summary, the ESIPT-based rhodamine-derived sensor **BHS** was successfully developed as

455 a multifunctional colorimetric and fluorescence probe for the selective detection of Cu^{2+} and

456 OCl$^-$ in aqueous solutions. The sensing mechanism involves the suppression of ESIPT followed

457 by spirolactam ring opening upon analyte interaction, leading to significant absorption and

458 emission shifts. The distinct spectral responses and large Stokes shifts further validate the

459 detection process. Additionally, the **BHS**-Cu^{2+} complex exhibited strong interactions with

460 biomolecules such as ct-DNA and BSA, as demonstrated by fluorescence titration studies and

461 molecular docking simulations. The structural optimization using DFT calculations provides

462 further insights into the binding behavior and electronic properties of the system. The variations

463 in fluorescence of **BHS** caused by Cu^{2+} and OCl$^-$ in biological samples were investigated

464 through the anticancer and biosensing activities of **BHS** in HCT-116 colorectal cancer cells.

465 These findings highlight the potential of **BHS** as an efficient chemosensor for environmental

466 and biological applications, particularly in metal ion and oxidative stress detection.

467 **4. Conflicts of interest**

468 There are no conflicts of interest to declare.

469 **5. Acknowledgements**

477 **6. References:**

478 1   S.-H. Park, N. Kwon, J.-H. Lee, J. Yoon and I. Shin, *Chem. Soc. Rev.*, 2020, **49**, 143–

479   179.

480 2   N. Esfandiari and M. Aliofkhazraei, *Talanta*, 2024, **277**, 126365.

481 3   L. Cui, J. Wu and H. Ju, *Biosens. Bioelectron.*, 2015, **63**, 276–286.

482 4   K. Sreenivasa Rao, T. Balaji, T. Prasada Rao, Y. Babu and G. R. K. Naidu, *Spectrochim.*

483   *Acta Part B At. Spectrosc.*, 2002, **57**, 1333–1338.

484 5   S. Khan, X. Chen, A. Almahri, E. S. Allehyani, F. A. Alhumaydhi, M. M. Ibrahim and

485   S. Ali, *J. Environ. Chem. Eng.*, 2021, **9**, 106381.

486 6   R. Sivakumar and N. Y. Lee, *BioChip J.*, 2021, **15**, 216–232.

487 7   W. Ma, R. Chen, T. Hu, S. Xing, G. Zhou, X. Qin, H. Ren, Z. Zhang, J. Chen and Q.

488   Niu, *Talanta*, 2023, **265**, 124910.

489 8   R. Chen, S. Xing, T. Hu, Y. Li, J. Chen, Q. Niu and T. Li, *Anal. Chim. Acta*, 2023, **1237**,

490   340557.

491 9   P. A. Kim, D. Choe, H. So, S. Park, B. Suh, S. Jeong, K.-T. Kim, C. Kim and R. G.

492   Harrison, *Spectrochim. Acta Part A Mol. Biomol. Spectrosc.*, 2021, **261**, 120059.

Materials Advances Accepted Manuscript

493 10   B. Bansod, T. Kumar, R. Thakur, S. Rana and I. Singh, *Biosens. Bioelectron.*, 2017, **94**,
494   443–455.

495 11   Z. Yan, Y. Cai, J. Zhang and Y. Zhao, *Measurement*, 2022, **187**, 110355.

496 12   F. Abebe, P. Perkins, R. Shaw and S. Tadesse, *J. Mol. Struct.*, 2020, **1205**, 127594.

497 13   E. Karakuş, *J. Mol. Struct.*, 2021, **1224**, 129037.

498 14   T. Chopra, S. Sasan, L. Devi, R. Parkesh and K. K. Kapoor, *Coord. Chem. Rev.*, 2022,
499   **470**, 214704.

500 15   S. Khan, X. Chen, A. Almahri, E. S. Allehyani, F. A. Alhumaydhi, M. M. Ibrahim and
501   S. Ali, *J. Environ. Chem. Eng.*, 2021, **9**, 106381.

502 16   S. B. Butt and M. Riaz, *J. Liq. Chromatogr. Relat. Technol.*, 2009, **32**, 1045–1064.

503 17   (a) S. Vishnu, A. Nag and A. K. Das, *Anal. Methods*, 2024, **16**, 5263. (b) G. C. Das, A.
504   K. Das, D. Das, T. R. Maity, A. Samanta, F. A. Alasmary, A. S. Almalki, A. Iqbal and
505   M. Dolai, *J. Photochem. Photobiol., A*, 2023, **440**, 114663 (c) S. Goswami, A. K. Das
506   and S. Maity, *Dalton Trans*., 2013, **42**, 16259–16263. (d) S. Vishnu, S. Maity, A. C.
507   Maity, S. K. Malavika, M. Dolai, A. Nag, Y. bylappa, G. Dutta, B. Mukherjee and A.
508   K. Das, *Spectrochim. Acta, Part A*, 2024, **315**, 124249. (e) S. Maity, A. C. Maity, A. k.
509   Das and N. Bhattacharyya, *Anal. Methods*, 2022, **14**, 2739–2744. (f) M. S. Kumar, S.
510   Pakrashy, S. Manna, S. M. Choudhury, B. Das, A. Ghosh, A. H. Seikh, M. Dolai and A.
511   K. Das, *Anal. Methods*, 2025, **17**, 2125-2133.

512 18   (a) V. S, A. K. Das, Y. Bylappa, A. Nag and M. Dolai, *Anal. Methods*, 2024, **16**, 8164–
513   8178. (b) A. K. Das, S. Goswami, C. K. Quah and H. K. Fun, *New J. Chem*., 2015, **39**,
514   5669–5675 (c) A. K. Das, N. Hayashi, Y. Shiraishi and T. Hirai, *RSC Adv*., 2017, **7**,
515   30453–30458. (d) A. K. Das, S. Goswami, C. K. Quah and H. K. Fun, *RSC Adv*., 2016,
516   **6**, 18711–18717. (e) A. K. Das, S. Goswami,G. Dutta, S. Maity, T. K. Mandal, K.
517   Khanra and N. Bhattacharyya, *Org. Biomol. Chem*., 2016, **14**, 570–576. (f) A. K. Das,
518   N. Hayashi, Y. Shiraishi and T. Hirai, *RSC Adv*., 2017, **7**, 30453–30458. (g) T. Das, E.
519   Joseph, M. S. Kumar, S. Vishnu, M. Dolai and A. K. Das, *Microchem. J.*, 2024, **199**,
520   110100. (h) M. S. Kumar, V. S., M. Dolai, A. Nag, Y. Bylappa and A. K. Das, *Anal.*
521   *Methods*, 2024, **16**, 676–685.

522 19   D. Xu, H. Jia, Y. Niu and S. Yin, *Dye. Pigment.*, 2022, **200**, 110185.

523   20   Y. Wang, X. Wang, W. Ma, R. Lu, W. Zhou and H. Gao, *Chemosensors*, 2022, **10**, 399.

524   21   S. Sarkar, A. Chatterjee and K. Biswas, *Crit. Rev. Anal. Chem.*, 2024, **54**, 2351–2377.

525   22   A. Mondal, S. Mukhopadhyay, E. Ahmmed, S. Banerjee, E. Zangrando and P.
526   Chattopadhyay, *J. Phys. Chem. C*, 2020, **124**, 18181–18193.

527   23   J. Guan, Q. Tu, L. Chen, M.-S. Yuan and J. Wang, *Spectrochim. Acta Part A Mol.*
528   *Biomol. Spectrosc.*, 2019, **220**, 117114.

529   24   (a)P.-T. Chou, Y.-C. Chen, W.-S. Yu, Y.-H. Chou, C.-Y. Wei and Y.-M. Cheng, *J. Phys.*
530   *Chem. A*, 2001, **105**, 1731–1740. (b) M. T. Ignasiak, C. Houee-Levin, G. Kciuk, B.
531   Marciniak and T. Pedzinski, *ChemPhysChem*, 2015, **16**, 628–633. (c) D. Ghosh, S.
532   Batuta, S. Das, N. A. Begum and D. Mandal, *J. Phys. Chem. B*, 2015, **119**, 5650–5661.
533   (d) S. J. Schmidtke, D. F. Underwood and D. A. Blank, *J. Am. Chem. Soc.*, 2004, **126**,
534   8620–8621. (e) M. J. Paterson, M. A. Robb, L. Blancafort and A. D. DeBellis, *J. Am.*
535   *Chem. Soc.*, 2004, **126**, 2912–2922. (f) E. Hadjoudis and I. M. Mavridis, *Chem. Soc.*
536   *Rev.*, 2004, **33**, 579–588. (g) Y. Nakane, T. Takeda, N. Hoshino, K. Sakai and T.
537   Akutagawa, *J. Phys. Chem. A*, 2015, **119**, 6223–6231.

538   25   P. Majumdar and J. Zhao, *J. Phys. Chem. B*, 2015, **119**, 2384–2394.

539   26   V. Dujols, F. Ford and A. W. Czarnik, *J. Am. Chem. Soc.*, 1997, **119**, 7386–7387.

540   27   M. Shortreed, R. Kopelman, M. Kuhn and B. Hoyland, *Anal. Chem.*, 1996, **68**, 1414–
541   1418.

542   28   H. A. Benesi and J. H. Hildebrand, *J. Am. Chem. Soc.*, 1949, **71**, 2703–2707.

543   29   Y. Shiraishi, Y. Kohno and T. Hirai, *Ind. Eng. Chem. Res.*, 2005, **44**, 847–851.

544   30   M. H. Lee, J. S. Kim and J. L. Sessler, *Chem. Soc. Rev.*, 2015, **44**, 4185–4191.

545   31   R. Bhowmick, A. S. M. Islam, U. Saha, G. Suresh Kumar and M. Ali, *New J. Chem.*,
546   2018, **42**, 3435–3443.

547   32. J. C. Stockert, R. W. Horobin, L. L. Colombo, A. Blázquez-Castro, *Acta histochemica*.
548   2018, 120, 159-67.

549   32   C. Kalaivanan, M. Sankarganesh, M. Y. Suvaikin, G. B. Karthi, S. Gurusamy, R.
550   Subramanian and R. N. Asha, *J. Mol. Liq.*, 2020, **320**, 114423.

551

- The data supporting this article have been included as part of the Supplementary Information.

Materials Advances Accepted Manuscript